International Journal of Refractory Metals and Hard Materials 113 (2023) 106200

Contents lists available at ScienceDirect

International Journal of Refractory Metals and Hard Materials

journal homepage: www.elsevier.com/locate/IJRMHM

VNbCrMo refractory high-entropy alloy for nuclear applications

P.A. Ferreirós [a,b,*], S.O. von Tiedemann [a], N. Parkes [a], D. Gurah [c], D.J.M. King [d], P. Norman [c], M. R. Gilbert [e], A.J. Knowles [a,d]

[a] School of Metallurgy and Materials, University of Birmingham, Birmingham B15 2TT, UK
[b] Comisión Nacional de Energía Atómica (CNEA), San Martín B1650KNA, Buenos Aires, Argentina
[c] School of Physics and Astronomy, University of Birmingham, Birmingham B15 2TT, UK
[d] Department of Materials, Imperial College London, Exhibition Road, South Kensington, SW7 1SZ, UK
[e] United Kingdom Atomic Energy Authority, Culham Centre for Fusion Energy, Abingdon OX14 3DB, UK

ARTICLE INFO

Keywords:
HEA
CCA
Refractory
VNbCrMo
BCC
C15 laves

ABSTRACT

Refractory high-entropy alloys (RHEAs) with high melting points and low neutron absorption cross-section are sought for generation-IV fission and fusion reactors. A high throughput computational screening tool, Alloy Search and Predict (ASAP), was used to identify promising RHEA candidates from over 1 million four-element equimolar combinations. The selected VNbCrMo RHEA was further studied by CALPHAD to predict phase formation, which was compared to an experimentally produced ingot aged at 1200 °C. The VNbCrMo RHEA was found to constitute a majority bcc phase, with a 6% area fraction of C15-Laves formed at interdendritic regions, in contrast to the predictions of single-phase. The prediction of the yield strength by a model based upon edge dislocation mechanisms indicated 2.1 GPa at room temperature and 850 MPa at 1000 °C for the equimolar single bcc phase. The hardness of the alloy with C15-Laves was 748 HV (yield strength ~2.4 GPa). Finally, the macroscopic neutron absorption cross-section was modelled for a wide range of energies. Displacements per atom per year and activation calculations, up to 1000 years after 2 years of continuous operation, in typical fusion and fission reactor scenarios were also performed using the inventory code FISPACT-II. This work gives new insight into the phase stability and performance of the VNbCrMo RHEA, which is compared with a similar design concept alloy, to assess the potential of novel RHEAs for use in advanced nuclear applications.

1. Introduction

High-temperature materials are critical to a wide array of advanced applications, including: gas turbines, rockets, hypersonics, and nuclear generation-IV fission and fusion reactors [1–4]. Extensive worldwide efforts are being made to devise new and ever improved materials that underpin increased reactor/engine performance and efficiency. High entropy alloys (HEAs, or multiple-principal element alloys MPEAs, or complex concentrated alloys CCAs) are a nascent materials class that have picked up extensive academic and industrial interest, particularly over the last ~10 years [5]. HEAs were first defined as alloys with at least five metallic elements and with each element between 5% and 35% atomic concentrations, but the restrictions of the composition-based definition were somewhat loosened and it is often found ternary or quaternary equimolar alloys referred to as HEAs [6]. Some HEAs are demonstrating exceptional properties like exceptional strength and ductility [7], lightweight in combination with high strength [8], and also remarkable irradiation damage tolerance [9]. A sub-class of HEAs that are seeing ever-increasing interest are refractory high-entropy alloys (RHEAs), as highlighted in Fig. 1a showing the rate of HEA and RHEA publications in recent years. However, a major challenge remains in how to efficiently screen the vast composition space of HEAs to find viable alloys and further how to quickly evaluate and optimise their properties.

In order to predict the formation of solid solutions in HEAs, King et al. [10] presented new empirical criteria based on two parameters and which improves the previous criteria from Yang et al. [11], which did not consider the enthalpies of formation of intermetallics and solid solutions. Firstly, King et al. maintain the widely used condition where the radius mismatch between elements is limited to values of $\delta < 6.6\%$ (see Eq. 1). Then, the other parameter that was introduced considers the ratio between the change in Gibbs free energy of formation of the disordered solid solution, ΔG_{ss}, and the intermetallic or segregated binary constitutes, ΔG_{max}. This empirical parameter, Φ (see Eq. 2), predicts a stable

* Corresponding author at: School of Metallurgy and Materials, University of Birmingham, Birmingham B15 2TT, UK.
E-mail address: p.ferreiros@bham.ac.uk (P.A. Ferreirós).

https://doi.org/10.1016/j.ijrmhm.2023.106200
Received 26 October 2022; Received in revised form 2 March 2023; Accepted 15 March 2023
Available online 17 March 2023

solid solution at the melting temperature of the system for values of $\Phi \geq 1$.

The Alloy Search and Predict (ASAP) [10] code was used as a screening tool to calculate the parameters δ and Φ for quaternary equiatomic mixtures. This calculation was performed with 72 elements from the periodic table (see Fig. 1a), resulting in 1,028,790 combinations [12]. Fig. 1b is shown by the shaded area that only a small number of equimolar quaternary alloys have the possibility to form single-phase solid solutions at high temperatures based on the criteria of ref. [10]. Within this small group of alloys, we set some requirements to select an alloy to further study experimentally. The first condition is to possess a low value of microscopic thermal neutron absorption cross-section in order to enable nuclear applications. The second condition is to use elements with melting temperatures below 2700 °C, or differences between the melting points of the elements below 1000 °C. We have set this condition to minimise macrosegregation effects produced by electric arc melting. The equimolar composition meeting the above requirements is the VNbCrMo alloy (see the selected elements on the periodic table of Fig. 2a). As shown in Fig. 1b, the VNbCrMo alloy is within the group of single-phase solid-solution formability with the values of $\delta = 4.83\%$ and $\Phi = 1.39$. The microscopic thermal neutron absorption cross-section of the VNbCrMo alloy is 2.94 b. This value makes it very attractive for nuclear applications, for example when compared to the VNbTiZr alloy (3.13 b) or 316 stainless steel (3.04 b) [10]. On the other hand, while the 4 elements of this alloy are attractive for their low neutron absorption cross-section, the Nb and Mo present a problem due to their high activation under neutron irradiation in fusion reactor environments [13]. Therefore, this alloy has limited application for fusion reactors from a long-lived hazardous radioactive waste point of view [14]. Finally, concerning producing an alloy without significant problems by electric arc melting, Fig. 2b shows that the four elements of the VNbCrMo alloy have melting points with smaller differences than 1000 °C and at the same time they do not reach melting temperatures as high as Ta.

Additionally, the high Cr content will promote protective oxide scale formation, suggesting potential applications in hot, oxidising environments [16]. An example of this was the improved corrosion resistance in dry air at high temperatures when V was replaced by Cr in the VNbTiZr alloy [17].

2. Materials and methods

Web of Science was used as a search engine to explore the publications trend of HEAs and refractory HEAs. The period 2004 to 2021 was analysed, considering English language journals and proceedings papers. The Alloy Search and Predict code (ASAP) [10] was used for screening potential alloys with single-phase stability at high temperatures (Fig. 1b). Among this group of possible alloys, the VNbCrMo alloy was chosen due to its low thermal microscopic neutron cross-section. Phase equilibrium calculation was performed by Calphad method with Thermocalc™. The phase equilibrium of the VNbCrMo alloy was predicted between 500 and 2750 °C using the TCHEA5 database.

A 7 g ingot of the equimolar VNbCrMo alloy was produced by electric arc melting with a tungsten electrode and a water-cooled copper crucible under an argon atmosphere. The chamber was evacuated, Ar-backfilled and a Ti lump melted as a remaining gas getter. The ingot was prepared by elemental metals with purity ≥99.9% and the obtained composition is given in Table 1. The as-cast ingot, wrapped in Mo foil and encapsulated in a silica glass evacuated and backfilled with Ar gas, was heat treated at 1200 °C for 100 h and water quenched. The surface for Electron Backscatter Diffraction (EBSD) scans was prepared by grinding and polishing with SiC papers and colloidal silica. Scanning Electron Microscopy (SEM), operated at 20 kV, was performed in a Jeol 7000F with Oxford Inca Energy-dispersive X-ray spectroscopy (EDS) and crystal EBSD. A misorientation angle threshold of 10° was used to indicate grain boundaries in EBSD maps. The alloy chemical composition was obtained as the average of four widely spaced EDS areas larger than 1 mm^2 along a central slice of the heat-treated ingot. The phase compositions were made by averaging six points of EDS measurements. The dispersions of the EDS chemical average compositions are indicated in the reported results. X-ray diffraction (XRD) pattern was taken on a Proto AXRD benchtop diffractometer (Cu Kα radiation) with a step size of 0.015° and sample holder spinning. The background was subtracted in the presented XRD spectrum. Hardness was measured by Vickers indentation using a 1000 g load in a Mitutoyo HM-124. The results are the average and standard deviation from five indentations along the ingot.

The modelling of the macroscopic neutron absorption cross-section of the alloys was calculated as a mixture of isotopes by summing the individual macroscopic cross-sections of the constituent elements in the material. The methodology used in the neutronic modelling couples OpenMC (version 0.12.0-dev) neutronic transport code with a bespoke python script to calculate the macroscopic neutron absorption cross-section for each alloy. The OpenMC code was used with the ENDF-B-VII.1 nuclear data library for neutrons at a fixed room temperature of 20 °C (294 K) to compute the individual macroscopic neutron absorption cross-sections.

The inventory code FISPACT-II [18] was used, in combination with the TENDL-2021 [19] nuclear data library, to predict neutron activation of the VNbCrMo and VNbTiZr alloys, as well as stainless steel (SS) 316

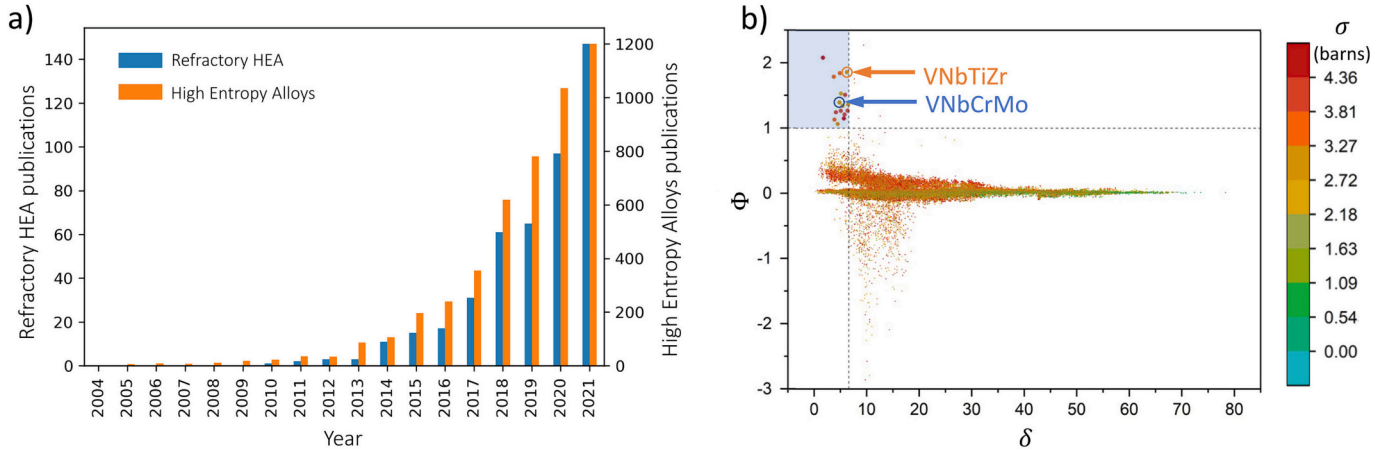

Fig. 1. (a) Historical evolution of articles about HEAs & RHEAs. (b) Parameters to predict the single-phase solid-solution formability from a previous thermodynamic assessment (Image adapted from ref. [12]). The shaded area indicates the possible formation of solid-solution alloys at high temperatures. The microscopic thermal neutron absorption cross-section is additionally indicated by the colour scale.

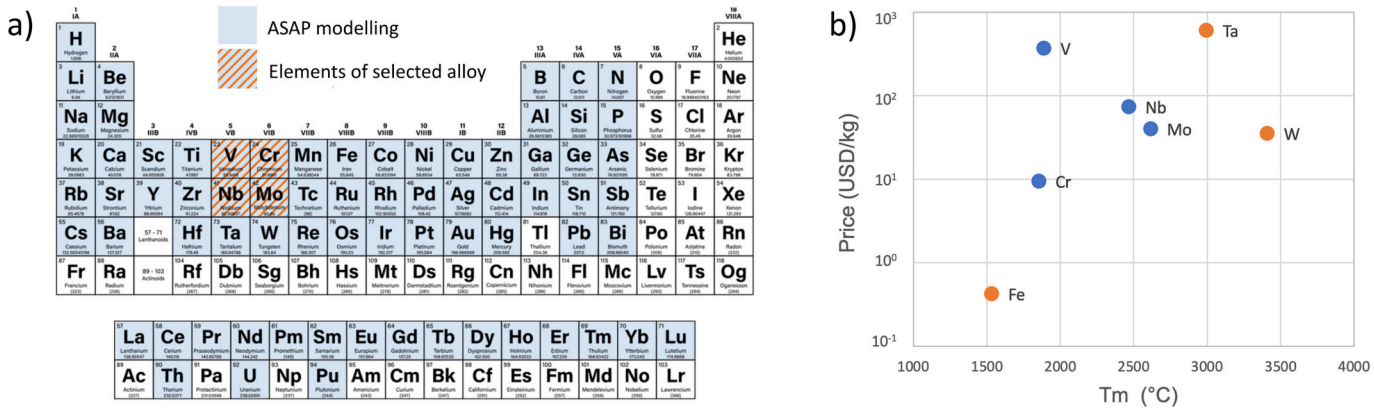

Fig. 2. (a) Periodic table highlighting the elements used for the RHEA in the present work and the 72 elements considered by ASAP modelling. (b) Price and melting temperature (Tm) of bcc metals (*data from Knowles* et al. [15]*)*.

Table 1
VNbCrMo alloy composition nominal, and measured by SEM-EDS area scans.

Composition (at.%)	V	Nb	Cr	Mo
Nominal	25.0	25.0	25.0	25.0
Measured	26.1 ± 0.3	25.4 ± 0.3	24.2 ± 0.4	24.4 ± 0.4

for comparison. Activation calculations for each material were performed with neutron spectra equivalent to exposure in (1) the first wall of the DEMOnstration (DEMO-FW) fusion power plant [20], (2) a fast-breeder reactor (FBR) core assembly, and (3) an averaged fuel assembly of a pressurized water reactor (PWR), as taken from [21].

Additionally, the displacements per atom (dpa) per year were calculated with FISPACT-II, using the Norgett-Robinson-Torrens (NRT) method [22]. Here, the total displacement rate is estimated as the concentration-weighted sum of the displacement rates (calculated using KERMA, Kinetic Energy Released per unit MAss, displacement cross sections) of individual elements making up the initial (before irradiation) compositions of the materials.

3. Results and discussion

In order to predict the thermodynamic stability of single-phase solid solution in HEAs we apply the criteria of King et al. [10], mentioned previously in the introduction ($\delta < 6.6\%$ and $\Phi \geq 1$). The two required parameters are calculated as follows,

$$\delta\,[\%] = \sqrt{\sum_{i=1}^{n} C_i\left(1 - \frac{r_i}{\bar{r}}\right)^2}\, x100 \tag{1}$$

Where C_i is the atomic percentage of the ith component r_i is the atomic radius of element i and $\bar{r}$ is the atomic radius average of the system.

$$\Phi = \frac{\Delta G_{ss}}{-|\Delta G_{max}|} \tag{2}$$

where ΔG_{ss} and $|\Delta G_{max}|$ are the change in Gibbs free energy of formation for the solid-solution and the maximum magnitude of a potential binary intermetallic compound (scaled to the number of elements in the solid-solution), respectively. To obtain $|\Delta G_{max}|$, all the possible binaries of the system must be considered. The ASAP code [10] was used as a screening tool to calculate the parameters of Eqs. (1) and (2). Fig. 1b shows a shaded area where only a small number of equimolar quaternary alloys have the possibility to form as a single-phase solid solution at high temperatures. The VNbCrMo alloy is within this group with values of $\delta = 4.83\%$ and $\Phi = 1.39$.

The phase equilibrium modelling for the VNbCrMo alloy is presented in Fig. 3. In accordance with ASAP, Thermocalc indicates a single-phase solid solution under the solidification temperature ($T_m \approx 2000$ °C). The modelling also shows a wide temperature range of a single bcc phase from T_m up to 1265 °C, where it begins a two-phase bcc field. This second bcc phase rapidly increases its molar fraction around 1200 °C and reaches approximately 50% at 500 °C.

The XRD spectrum of the VNbCrMo alloy with the thermal treatment at 1200 °C for 100 h is shown in Fig. 3b. This technique indicated the presence of two phases: a bcc and a C15-Laves. The intensities of the phase peaks in the XRD spectra indicate a low volume fraction of the C15-Laves phase, although the amount of phases is estimated further below by EBSD. Fig. 4a shows SEM micrographs of the treated alloy. A dendritic microstructure and a minority fraction of a second phase located in the interdendritic zones were found. The EDS composition mapping does not reflect appreciable differences in the elements of the majority (bcc) phase, but the second interdendritic phase has higher Cr and Nb content and reduced Mo and V (Fig. 4b). Table 2 shows the average composition of both phases. The bcc phase has higher Mo and lower Cr contents, although it is close to equimolar composition. The EBSD indexation confirmed a majority of the bcc phase and also the presence of a C15-Laves phase located at interdendritic zones (Fig. 4c). A volume fraction of 6% area of the C15-Laves phase was obtained from this measurement. These experimental results do not agree with the dual-bcc phase equilibrium obtained by Thermocalc modelling at 1200 °C (Fig. 3a).

Fig. 4c also shows the EBSD phase orientation map. Each interdendritic region where the Laves phase was formed, has a big number of finer grain sizes (sub-micron). This small grain size could be beneficial to increase the strengthening by Hall-Petch effect. Some authors indicated a reduction of ductility by increasing the volume fraction of Laves phase in HEAs but this effect was observed with higher values than in the present alloy [23,24].

A hardness of 7.34 ± 0.07 GPa was measured in the heat-treated alloy. According to Tabor's empirical relation: $\sigma_H \approx 3\sigma_{YS}$, where σ_H is the hardness and σ_{YS} the yield stress (YS), is possible to estimate an approximate value of 2.45 GPa yield stress. Recently, a theory supported by experiments in bcc RHEAs indicates that strength is controlled by edge dislocations. The strength-controlled mechanism was adopted by Maresca & Curtin to obtain an analytic theory that depends only on elastic moduli and misfit volumes for bcc HEAs [25]. The analytic theory can be easily applied to estimate the yield strength versus temperature and here we applied the code and data provided in the ref. [25] to calculate the yield stress of the VNbCrMo alloy from room temperature (RT) up to high temperatures. The applied parameters used in the model were the following: Taylor Factor of 3.067, non-dimensional parameter contained in the line tension calculation α=1/12 and strain rate of $1 \times 10^{-4}\ s^{-1}$. The result is shown in Fig. 5 and is compared with the YS at RT

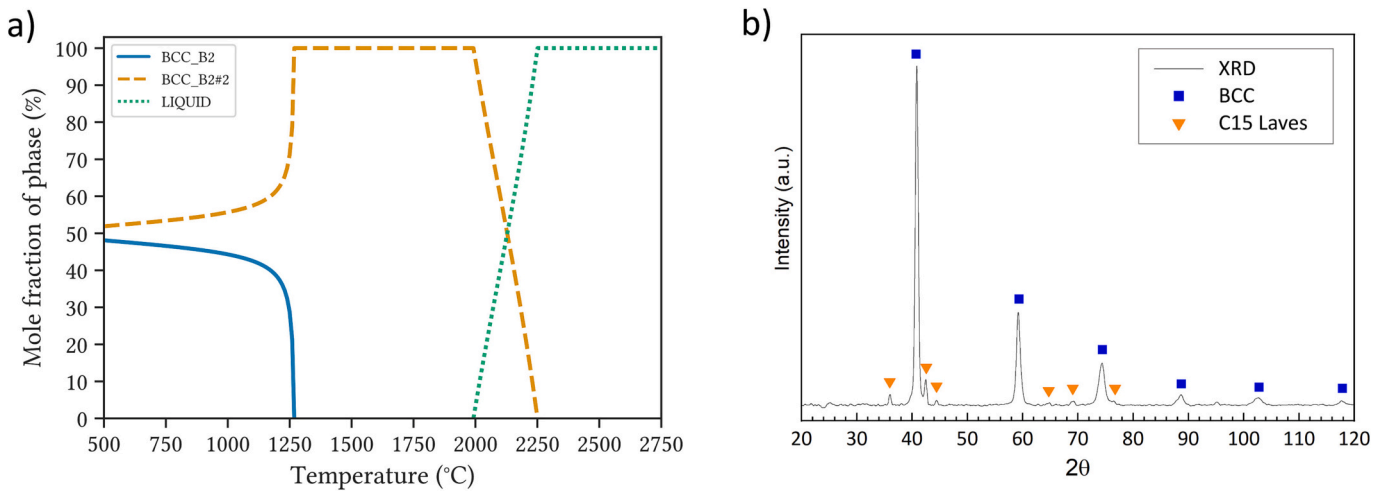

Fig. 3. VNbCrMo alloy (a) Phase equilibrium predicted by Thermocalc TCHEA5. b) XRD in the heat-treated alloy.

estimated from hardness by Tabor's relation. Additionally, the non-equiatomic composition measured in the bcc phase was modelled (see values in Table 2). It can be seen that the reduction of Cr and increase of Mo with respect to the equiatomic composition generate a slight drop in the yield stress. In other words, the formation of the C15-Laves phase reduces the yield strength of the bcc phase. On the other hand, the 6% volume fraction of sub-micron grain sizes of Laves phase at interdendritic zones is likely to generate a greater strengthening effect on yield stress than the modelled drop of the bcc phase. From Fig. 5 it can be seen that at room temperature the hardness measured in the VNbCrMo alloy reflects higher yield stress values than those predicted by the model for equimolar and non-equimolar single-phase bcc alloys. This indicates that the laves phase has a strengthening effect on the bcc phase. However, this speculation is valid as long as Tabor's relation is satisfied for this alloy and if the yield stress modelling is accurate. While future testing of the yield strength in the VNbCrMo alloy is required, based on the modelling of Fig. 5, it is possible to point out that this alloy has a promising high strength (above 2.1 GPa at RT and 850 MPa at 1000 °C).

Since the key design factor in the selection of the VNbCrMo HEA for nuclear applications was its low thermal neutron absorption cross-section, it is necessary to discuss in this framework its behaviour with respect to other HEAs. The VNbTiZr HEA was identified as a potential candidate for fusion application due to its low microscopic thermal neutron absorption cross-section [12], and as mentioned in the introduction, it has a 7% higher value than the VNbCrMo alloy. However, the property that best represents the neutron transparency is the macroscopic neutron absorption cross-section. This property in addition takes into account the alloy's density, and for the VNbCrMo and VNbTiZr comparison, a lower value is obtained for the latter alloy. Fig. 6 shows this property for a wide range of energies for both HEAs and a stainless steel. From the modelling, it is observed that the VNbCrMo alloy has a slightly higher resonance than the VNbTiZr alloy, and although the neutron absorptions are similar, the latter alloy is slightly better.

From a wider point of view, the VNbTiZr alloy has a much higher neutron absorption cross-section than Zr-base alloys, and in reference [26] it is mentioned that the higher yield strength of this HEA could be high enough to allow a reduction in the structural fraction application which result in a low total neutron absorption like the Zr-base alloys. Therefore, with this same concept of analysis, considering the higher yield strength of the VNbCrMo alloy with respect to VNbTiZr (Fig. 5b), the VNbCrMo alloy will require much thinner sections than the VNbTiZr alloy to withstand the same load. Finally, due to their similar neutron absorptions, the VNbCrMo alloy will result in considerably higher neutron transparency.

Additional factors not taken into account in the design of the VNbCrMo alloy but which are key for analysing the potential applications of nuclear materials are the radiological, transmutation, and damage responses under reactor environments. With this aim, FISPACT-II was used to predict the expected behaviour of the RHEA in some hypothetical nuclear reactor scenarios: fusion DEMO-FW, an FBR, and a PWR.

Fig. 7a shows the total activity 1000 years after 2 full-power year (fpy) irradiations in DEMO-FW, FBR and PWR environments for VNbCrMo, VNbTiZr and SS316 alloys. It should be noted that because of the elements used in the three alloys, none of them can be expected to meet the low-level radioactive waste (LLW) requirements of future fusion reactors, a target UK fusion programmes aim to meet (12 MBq/kg after 100 years) [27,28]. We are comparing both RHEAs with the SS316 alloy because it is a widely used structural material, however, this SS316 was never intended to be used as FW in a fusion reactor, and we do not suggest that this is a limitation to its potential fission applications. Analysing the VNbCrMo alloy for DEMO-FW, Fig. 7b, shows that the most concerning nuclides (the ones that dominate at long decay times) are created by nuclear reactions on Nb (^{93m}Nb, ^{91}Nb, ^{94}Nb) and Mo (^{93}Mo and ^{99}Tc). The VNbTiZr alloy, Fig. 7c, has a high activity contribution from the same three Nb nuclides, but is predicted to have a slighter lower total activity at long-decay times due to the absence of Mo in its composition. If a RHEA is desired for fusion, it would be advisable, and may even be required from a regulatory perspective due to the ALARP (as low as reasonably practicable) principle, to avoid or reduce the content of Nb and Mo to minimise the level of radioactive waste. As well as the substitution of these elements, one possible approach to reducing the activity of a RHEA is by isotopic adjustment of those elements [29]. These results highlight the demanding challenges of designing alloys for nuclear applications with sufficient mechanical and structural performance while at the same time minimising the cost of waste disposal and decommissioning after end-of-life [30,31].

In order to compare the structural damage dose that would be experienced by the alloys, FISPACT-II was also used to model NRT-dpa/year in the alloys in the same nuclear reactor scenarios mentioned previously. Fig. 8 shows the dpa/year estimated by the concentration-weighted sum of the dpa rates of the constituents for the initial compositions of the RHEA and SS316. The alloys have similar orders of dpa/year rates, although VNbTiZr is the alloy with slightly higher damage of the three.

In view of future work, exploration at higher ageing temperatures would be useful to prove the existence of a single-phase equilibrium field in the VNbCrMo alloy. Specifically for use of the alloy in nuclear applications, the radiation damage resistance will be an essential topic of future investigation and validation. Regarding mechanical properties,

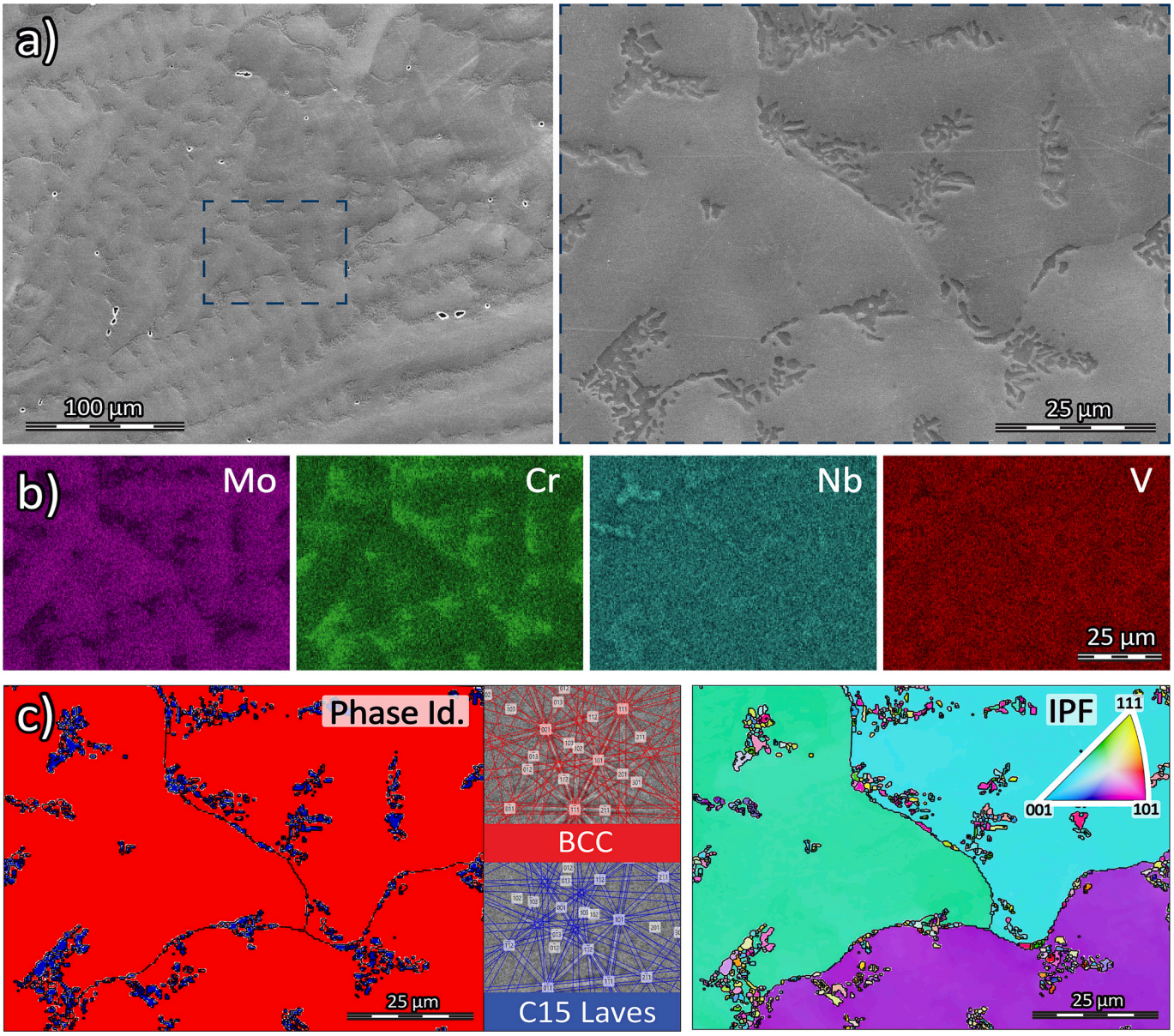

Fig. 4. VNbCrMo aged alloy (a) Secondary electrons micrographs in SEM at low and higher magnifications (inset showing the area analysed by the following techniques). (b) EDS composition maps. (c) phase identification and phase orientation maps by EBSD.

Table 2
Chemical phase compositions (at.%) by EDS in the aged VNbCrMo alloy.

Phase	Morphology/ Location	V	Nb	Cr	Mo
Matrix BCC	Dendrites	24.3 ± 1.0	25.7 ± 0.4	19.5 ± 1.2	30.5 ± 1.8
Laves C15	Interdendritic zone	16.8 ± 0.4	30.9 ± 0.2	47.1 ± 0.9	5.2 ± 0.8

strength and ductility up to high temperatures and the ductile-to-brittle temperature transition, are needed in order to demonstrate the suitability of these novel low neutron absorption cross-section RHEA.

4. Conclusion

The VNbCrMo RHEA was computationally selected from a group of quaternary equimolar alloys predicted to be a single-phase at high temperatures by the ASAP code. The additional characteristics for selecting this RHEA were the low microscopic thermal neutron cross-section (2.94 b) and the similarity of melting temperatures between the elements, which at the same time do not exceed 2700 °C. These characteristics are critical for neutron efficiency in nuclear applications and to reduce the macrosegregation by electric arc melting production.

Equilibrium phase modelling for the VNbCrMo was performed using Thermocalc that predicted a single-phase bcc solid-solution from the solidus temperature (2000 °C) down to 1265 °C, below which a two-phase bcc miscibility gap is predicted. In contrast, the experimental techniques (XRD and EBSD) on the VNbCrMo alloy treated at 1200 °C showed a majority bcc phase, but with a low percentage of C15-Laves (~6% area). The Laves phase was formed at the interdendritic zones, with fine grain sizes (sub-micron).

The VNbCrMo alloy shows a hardness of 7.34 GPa, which indicate high yield stress at room temperature (about 2.45 GPa). A yield strength modelling based on edge dislocation mechanism predicts 2.1 GPa at room temperature and 850 MPa at 1000 °C for a single bcc phase alloy with equimolar composition.

Finally, the macroscopic neutron absorption cross-section was

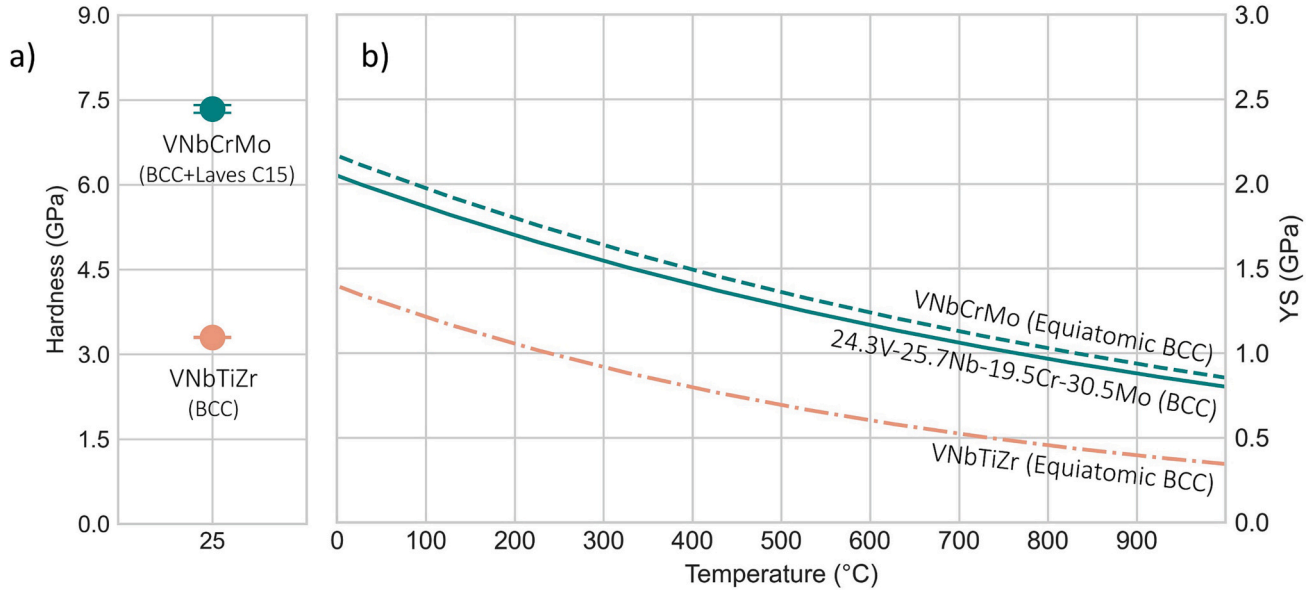

Fig. 5. Hardness at RT, and yield stress (YS) for VNbCrMo and VNbTiZr [12] alloys. The ratio between vertical axes of both graphs maintains the Tabor's relation ($\sigma_H \approx 3\sigma_{YS}$). a) Hardness by Vickers indentation. b) Modelling of YS vs temperature for single-phase bcc alloys with equimolar compositions and the non-equimolar composition measured in the bcc phase by EDS (see Table 2). Modelling code from ref. [25].

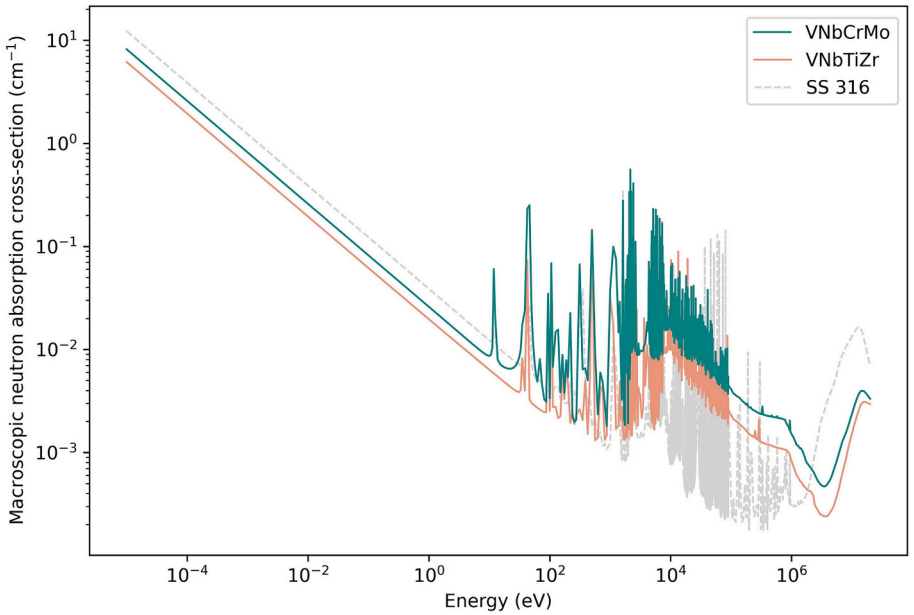

Fig. 6. Macroscopic neutron absorption cross-section for different energies modelled by ENDF-B-VII.1 nuclear data library at a fixed room temperature of 294 K (Reaction: MT = 101 (n, disappear)) for VNbCrMo, NbZrTiV and 316 stainless steel.

modelled for a wide range of energies and together with the yield strength predictions, the alloy was compared with a similar design concept RHEA (VNbTiZr), and with a structural SS316 to assess the potential for advanced nuclear applications. Activation of the RHEAs is expected to be a problem if it is desired that the alloys should be disposable as low-level waste (LLW) within 100 years post-operation. This is predominantly due to the inclusion of Nb and Mo, leading to the production of long-lived radioisotopes of those elements. The displacements per atom (dpa) per year predictions do not suggest any major limitations to the use of these RHEAs, however, experimental studies are required to develop an understanding of their radiation tolerances.

CRediT authorship contribution statement

P.A. Ferreirós: Conceptualization, Methodology, Formal analysis, Investigation, Writing – original draft, Writing – review & editing. **S.O. von Tiedemann:** Software, Formal analysis, Investigation, Writing – original draft. **N. Parkes:** Formal analysis, Investigation. **D. Gurah:** Investigation, Writing – original draft. **D.J.M. King:** Software, Investigation. **P. Norman:** Investigation, Writing – review & editing, Supervision. **M.R. Gilbert:** Software, Investigation, Data curation, Writing – review & editing, Supervision. **A.J. Knowles:** Conceptualization, Writing – review & editing, Supervision, Funding acquisition.

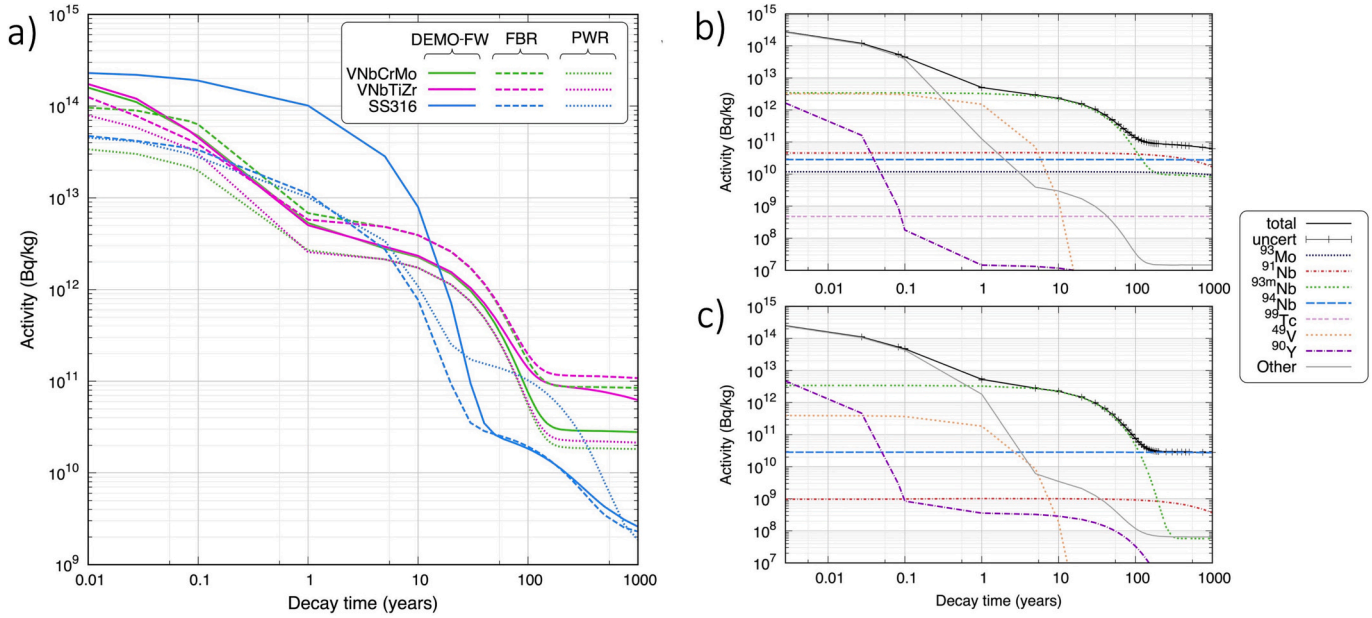

Fig. 7. Activity evolution in VNbCrMo, VNbTiZr and SS316 following 2 full-power year (fpy) irradiations under three scenarios: the first wall (FW) of DEMO fusion reactor, a fast-breeder reactor (FBR), and pressurized water-cooled reactor (PWR). a) Total decay response. Nuclide contributions in the FW of DEMO for: b) VNbCrMo and c) VNbTiZr alloys. Only dominant nuclides with activity above 12 MBq/kg after 10 years of decay were plotted individually. All other nuclides are summarised in the respective "other" curve.

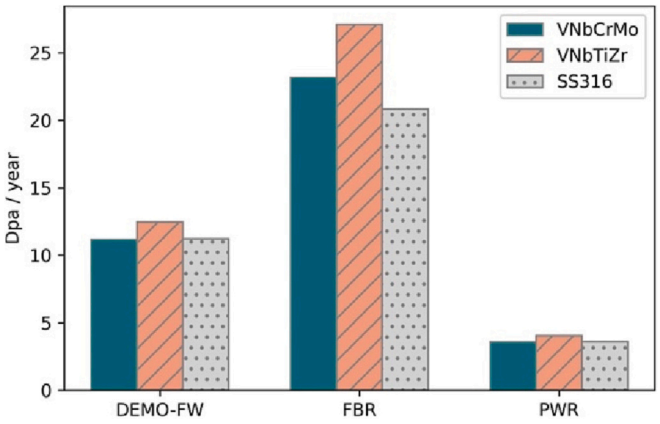

Fig. 8. Displacements per atom (dpa) per year for the nominal composition of VNbCrMo, VNbTiZr and SS316 alloys under FW-DEMO, PWR and FBR scenarios.

Declaration of Competing Interest

The authors declare that they have no known competing financial interests or personal relationships that could have appeared to influence the work reported in this paper.

Data availability

Data will be made available on request.

Acknowledgements

A.J. Knowles and P.A. Ferreirós gratefully acknowledge funding from EPSRC (EP/T01220X/1). A.J. Knowles gratefully acknowledges funding from a UKRI Future Leaders Fellowship (MR/T019174/1) and Royal Academy of Engineering Research Fellowship (RF\201819\18 \158), and EUROfusion Research Grant (AWP17-ERG-CCFE/Knowles). The authors gratefully acknowledge the Centre for Electron Microscopy (University of Birmingham) for their support & assistance in this work. M.R. Gilbert acknowledges funding from the EPSRC Energy Programme (EP/W006839/1).

References

[1] X.-J. Hua, P. Hu, H.-R. Xing, J.-Y. Han, S.-W. Ge, S.-L. Li, C.-J. He, K.-S. Wang, C.-J. Cui, Development and property tuning of refractory high-entropy alloys: a review, Acta Metall. Sin. (Engl. Lett.) 35 (2022) 1231–1265, https://doi.org/10.1007/s40195-022-01382-x.

[2] A.O. Moghaddam, A. Cabot, E.A. Trofimov, Does the pathway for development of next generation nuclear materials straightly go through high-entropy materials? Int. J. Refract. Met. Hard Mater. 97 (2021), 105504 https://doi.org/10.1016/j.ijrmhm.2021.105504.

[3] Y. Zhang, T.T. Zuo, Z. Tang, M.C. Gao, K.A. Dahmen, P.K. Liaw, Z.P. Lu, Microstructures and properties of high-entropy alloys, Prog. Mater. Sci. 61 (2014) 1–93, https://doi.org/10.1016/j.pmatsci.2013.10.001.

[4] J. Han, B. Su, J. Meng, A. Zhang, Y. Wu, Microstructure and composition evolution of a fused slurry silicide coating on MoNbTaTiW refractory high-entropy alloy in high-temperature oxidation environment, Materials 13 (2020) 3592, https://doi.org/10.3390/ma13163592.

[5] E.P. George, D. Raabe, R.O. Ritchie, High-entropy alloys, Nat. Rev. Mater. 4 (2019) 515–534, https://doi.org/10.1038/s41578-019-0121-4.

[6] W. Li, D. Xie, D. Li, Y. Zhang, Y. Gao, P.K. Liaw, Mechanical behavior of high-entropy alloys, Prog. Mater. Sci. 118 (2021), 100777, https://doi.org/10.1016/j.pmatsci.2021.100777.

[7] Z. Li, K.G. Pradeep, Y. Deng, D. Raabe, C.C. Tasan, Metastable high-entropy dual-phase alloys overcome the strength–ductility trade-off, Nature 534 (2016) 227–230, https://doi.org/10.1038/nature17981.

[8] R. Feng, C. Zhang, M.C. Gao, Z. Pei, F. Zhang, Y. Chen, D. Ma, K. An, J. D. Poplawsky, L. Ouyang, Y. Ren, J.A. Hawk, M.L. Widom, P.K. Liaw, High-throughput design of high-performance lightweight high-entropy alloys, Nat. Commun. 12 (2021) 4329, https://doi.org/10.1038/s41467-021-24523-9.

[9] O. El-Atwani, N. Li, M. Li, A. Devaraj, J.K.S. Baldwin, M.M. Schneider, D. Sobieraj, J.S. Wróbel, D. Nguyen-Manh, S.A. Maloy, E. Martinez, Outstanding radiation resistance of tungsten-based high-entropy alloys, Sci. Adv. 5 (2019), https://doi.org/10.1126/sciadv.aav2002 eaav2002.

[10] D.J.M. King, S.C. Middleburgh, A.G. McGregor, M.B. Cortie, Predicting the formation and stability of single phase high-entropy alloys, Acta Mater. 104 (2016) 172–179, https://doi.org/10.1016/j.actamat.2015.11.040.

[11] H. Yang, C. Yang, Prediction of high-entropy stabilized solid-solution in multi-component alloys, Mater. Chem. Phys. 132 (2012) 233–238, https://doi.org/10.1016/j.matchemphys.2011.11.021.

[12] D.J.M. King, S.T.Y. Cheung, S.A. Humphry-Baker, C. Parkin, A. Couet, M.B. Cortie, G.R. Lumpkin, S.C. Middleburgh, A.J. Knowles, High temperature, low neutron cross-section high-entropy alloys in the Nb-Ti-V-Zr system, Acta Mater. 166 (2019) 435–446, https://doi.org/10.1016/j.actamat.2019.01.006.

[13] E.J. Pickering, A.W. Carruthers, P.J. Barron, S.C. Middleburgh, D.E.J. Armstrong, A.S. Gandy, High-entropy alloys for advanced nuclear applications, Entropy 23 (2021) 98, https://doi.org/10.3390/e23010098.
[14] M.R. Gilbert, T. Eade, T. Rey, R. Vale, C. Bachmann, U. Fischer, N.P. Taylor, Waste implications from minor impurities in European DEMO materials, Nucl. Fusion 59 (2019), 076015, https://doi.org/10.1088/1741-4326/ab154e.
[15] A.J. Knowles, D. Dye, R.J. Dodds, A. Watson, C.D. Hardie, S.A. Humphry-Baker, Tungsten-based bcc-superalloys, Appl. Mater. Today 23 (2021), 101014, https://doi.org/10.1016/j.apmt.2021.101014.
[16] D. Ikeuchi, D.J.M. King, K.J. Laws, A.J. Knowles, R.D. Aughterson, G.R. Lumpkin, E.G. Obbard, Cr-Mo-V-W: a new refractory and transition metal high-entropy alloy system, Scr. Mater. 158 (2019) 141–145, https://doi.org/10.1016/j.scriptamat.2018.08.045.
[17] T.M. Butler, K.J. Chaput, J.R. Dietrich, O.N. Senkov, High temperature oxidation behaviors of equimolar NbTiZrV and NbTiZrCr refractory complex concentrated alloys (RCCAs), J. Alloys Compd. 729 (2017) 1004–1019, https://doi.org/10.1016/j.jallcom.2017.09.164.
[18] J.-Ch. Sublet, J.W. Eastwood, J.G. Morgan, M.R. Gilbert, M. Fleming, W. Arter, FISPACT-II: An advanced simulation system for activation, transmutation and material modelling, Nucl. Data Sheets 139 (2017) 77–137, https://doi.org/10.1016/j.nds.2017.01.002.
[19] A.J. Koning, D. Rochman, J.-Ch. Sublet, TENDL-2021 (2021), Release Date: December 30, Available from, https://tendl.web.psi.ch/tendl_2021/tendl2021.html, 2021.
[20] G. Federici, R. Kemp, D. Ward, C. Bachmann, T. Franke, S. Gonzalez, C. Lowry, M. Gadomska, J. Harman, B. Meszaros, C. Morlock, F. Romanelli, R. Wenninger, Overview of EU DEMO design and R&D activities, Fusion Eng. Des. 89 (2014) 882–889, https://doi.org/10.1016/j.fusengdes.2014.01.070.
[21] M.R. Gilbert, J.-Ch. Sublet, Scoping of material response under DEMO neutron irradiation: comparison with fission and influence of nuclear library selection, Fusion Eng. Des. 125 (2017) 299–306, https://doi.org/10.1016/j.fusengdes.2017.06.016.
[22] M.J. Norgett, M.T. Robinson, I.M. Torrens, A proposed method of calculating displacement dose rates, Nucl. Eng. Des. 33 (1975) 50–54, https://doi.org/10.1016/0029-5493(75)90035-7.
[23] O.N. Senkov, S. Rao, K.J. Chaput, C. Woodward, Compositional effect on microstructure and properties of NbTiZr-based complex concentrated alloys, Acta Mater. 151 (2018) 201–215, https://doi.org/10.1016/j.actamat.2018.03.065.
[24] C. Xiang, H.M. Fu, Z.M. Zhang, E.-H. Han, H.F. Zhang, J.Q. Wang, G.D. Hu, Effect of Cr content on microstructure and properties of $Mo_{0.5}VNbTiCr_x$ high-entropy alloys, J. Alloys Compd. 818 (2020), 153352, https://doi.org/10.1016/j.jallcom.2019.153352.
[25] F. Maresca, W.A. Curtin, Mechanistic origin of high strength in refractory BCC high entropy alloys up to 1900K, Acta Mater. 182 (2020) 235–249, https://doi.org/10.1016/j.actamat.2019.10.015.
[26] D.J.M. King, A.J. Knowles, D. Bowden, M.R. Wenman, S. Capp, M. Gorley, J. Shimwell, L. Packer, M.R. Gilbert, A. Harte, High temperature zirconium alloys for fusion energy, J. Nucl. Mater. 559 (2022), 153431, https://doi.org/10.1016/j.jnucmat.2021.153431.
[27] I. Cook, D. Maisonnier, N.P. Taylor, D.J. Ward, P. Sardain, L. Di Pace, L. Giancarli, S. Hermsmeyer, P. 942 Norajitra, R. Forrest & PPCS Team, European fusion power plant studies, Fusion Sci. Technol. 47 (2005) 384–392, https://doi.org/10.13182/FST05-A719.
[28] M.R. Gilbert, T. Eade, C. Bachmann, U. Fischer, N.P. Taylor, Activation, decay heat, and waste classification studies of the European DEMO concept, Nucl. Fusion 57 (2017), 046015, https://doi.org/10.1088/1741-4326/aa5bd7.
[29] M.R. Gilbert, L.W. Packer, T. Stainer, Experimental validation of inventory simulations on molybdenum and its isotopes for fusion applications, Nucl. Fusion 60 (2020), 106022, https://doi.org/10.1088/1741-4326/aba99c.
[30] R. Pampin, S. Zheng, S. Lilley, B.C. Na, M.J. Loughlin, N.P. Taylor, Activation analyses updating the ITER radioactive waste assessment, Fusion Eng. Des. 87 (2012) 1230–1234, https://doi.org/10.1016/j.fusengdes.2012.02.110.
[31] M.R. Gilbert, T. Eade, T. Rey, R. Vale, C. Bachmann, U. Fischer, N.P. Taylor, Waste implications from minor impurities in European DEMO materials, Nucl. Fusion 59 (7) (2019), 076015, https://doi.org/10.1088/1741-4326/ab154e.